Research Square

Preprints are preliminary reports that have not undergone peer review.
They should not be considered conclusive, used to inform clinical practice,
or referenced by the media as validated information.

Magnetic carbon aerogel catalyst for nitro reduction by a liquid organic hydrogen carrier, considering the effect of preparation method on catalytic activity

Anahita Arastofar
Isfahan University of Technology
Hossein Tavakol
h_tavakol@iut.ac.ir

Isfahan University of Technology

Article

Keywords: LOHC, Aerogel, Hydrogenation, Isopropanol, Nitroarene, CNT

Posted Date: July 10th, 2026

DOI: https://doi.org/10.21203/rs.3.rs-10203376/v1

License: This work is licensed under a Creative Commons Attribution 4.0 International License.
Read Full License

Additional Declarations: No competing interests reported.

Version of Record: A version of this preprint was published at Scientific Reports on November 10th, 2026. See the published version at https://doi.org/10.1038/s41598-026-79248-w.

Abstract

In this work, four types (A-D) of magnetic CNT–Fe_3O_4 aerogel catalyst was synthesized using four different preparation methods through the incorporation of Fe_3O_4 nanoparticles into a chitosan- or PVA-crosslinked carbon nanotube network and applied to the transfer hydrogenation of nitroarenes using isopropanol as a liquid organic hydrogen carrier (LOHC). The structure and properties of the prepared catalysts were characterized by FTIR, XRD, Raman spectroscopy, FESEM, EDS, BET, TGA, contact angle measurements, and VSM analysis. For the selected catalyst (D), the catalytic activity was evaluated in the reduction of nitrobenzene under a nitrogen atmosphere, and an aniline yield of 72% was obtained under the optimized conditions using 20 mg of catalyst, 3 equivalents of NaOH, and 5 mL of isopropanol under reflux conditions. The applicability of the catalytic system was further investigated using 24 nitroarene derivatives, affording moderate to good yields, particularly for halogen-substituted substrates. Furthermore, the catalyst was readily separated from the reaction medium using an external magnet and reused for four consecutive cycles with only a slight decrease in catalytic activity.

Introduction

Nitroarene hydrogenation to aromatic amines is a key transformation in organic synthesis, as anilines serve as essential intermediates in the production of pharmaceuticals, agrochemicals, dyes, polymers, and specialty chemicals. The conversion of nitroarenes into aniline derivatives remains a major focus in academic research and industrial applications. Conventional reduction methods based on stoichiometric reagents such as sulfides, iron, and zinc are widely used at the industrial scale; however, they generate large quantities of acidic waste and solid by-products, raising significant environmental and sustainability concerns. In this context, catalytic hydrogenation has emerged as a more efficient and environmentally benign alternative [1–6]. Among the available approaches, catalytic reduction by hydrogen transfer using hydrogen donors, especially liquid organic hydrogen carriers (LOHCs) such as 2-propanol, offers a safer and operationally simpler route than high-pressure molecular hydrogen systems, which require specialized equipment and involve safety limitations [7–9].

2-Propanol is extensively used as both a hydrogen donor and solvent due to its affordability, availability, appropriate boiling point, and excellent solubility, while yielding acetone as an easily separable by-product [10, 11]. Several studies have illustrated its efficacy in the reduction of nitroarenes, including an iridium-catalyzed system that achieves nearly complete conversion of nitrobenzene [12], as well as magnetically recoverable heterogeneous systems employing noble-metal or graphene-supported catalysts [13]. Conversely, less efficient transformations have been observed in nonnoble metal systems [14], underscoring that catalytic performance is significantly influenced by the design of the support architecture and the accessibility of active sites. These observations suggest that the development of robust, cost-effective, and ligand-free catalytic systems using LOHCs remains a significant challenge.

Magnetic nanoparticles, particularly Fe_3O_4, have been widely investigated as a catalyst or catalyst supports due to their high surface area, chemical stability, low toxicity, and facile separation using an

external magnetic field. Despite these advantages, Fe_3O_4 nanoparticles are prone to oxidation and aggregation, which can reduce active surface accessibility and limit catalytic durability. Therefore, the development of structured supports capable of stabilizing Fe_3O_4 while maintaining high catalytic accessibility is crucial for improving system performance [15–20].

In this regard, carbon-based aerogels, offer a promising solution since they consist of an ultralight 3D network in which carbon nanotubes are interconnected through van der Waals interactions, resulting in extremely high porosity (≈ 90–99% gas phase). CNTs are attractive catalyst supports because of their high electrical and thermal conductivity, mechanical strength, and facile surface functionalization. Importantly, their one-dimensional structure can suppress magnetic nanoparticle aggregation and improve the dispersion of active species. However, mechanically weak inter-tube interactions often lead to structurally fragile aerogels with limited elasticity and poorly stabilized frameworks. As a result, additional structural reinforcement is typically required to obtain mechanically stable and functional catalytic architectures [21–26]. Making aerogels from CNT, needs to an appropriate crosslinker, which can be obtained from the neural compounds such as chitosan. Chitosan, a naturally abundant polysaccharide, provides an effective strategy for addressing this limitation due to its inherent ability to form cross-linked 3D networks thought amino and hydroxyl functional groups. These functional groups enable strong interactions with functionalized CNTs, promoting the formation of mechanically stable hybrid aerogels. In addition, chitosan acts as a structural binder that enhances network integrity and provides additional coordination/anchoring sites for the immobilization of catalytic nanoparticles. Consequently, chitosan/CNT hybrid aerogels represent a multifunctional platform that integrates mechanical stability, high porosity, and functional versatility for catalyst design [27–31].

Despite extensive progress in magnetic catalyst supports and carbon-based aerogels, the rational integration of Fe_3O_4 nanoparticles into chitosan/CNT aerogel frameworks for catalytic transfer hydrogenation systems using 2-propanol has received limited systematic investigation, particularly in terms of understanding how support architecture and Fe_3O_4 dispersion collectively influence catalytic performance and recyclability. Herein, after the previous efforts of this research group and the catalytic reaction, based on carbon aerogels [32–34], we address this challenge by designing Fe_3O_4-decorated chitosan/CNT aerogels through controlled magnetite incorporation strategies and varying Fe_3O_4-to-CNT ratios. The relationship between structural composition and catalytic performance was systematically investigated to identify the optimal catalyst configuration. The resulting material was applied for the transfer hydrogenation of nitroaromatic compounds using 2-propanol as a hydrogen donor under mild conditions. In contrast to conventional noble metal-based systems, this catalytic platform relies on low-cost and readily available components. The synergistic integration of a recyclable magnetic phase, a mechanically reinforced porous aerogel network, and a benign hydrogen donor provides a rationally designed catalytic system for efficient nitroarene reduction.

Result and discussion

Catalyst characterization

To study the effect of preparation method on the catalytic activity, as it described in method section, four different methods were performed for preparation of catalyst, then all four catalysts were used in the reaction to examine them, and finally the best catalyst (D, based on Table 1) was chosen for the next experiments and analysis. In catalyst A (or sample A), first the mixing of nano magnetite and carboxylated CNT (named briefly as CNT) was performed, followed by chitosan addition and gelation. In catalyst B, first gelation was accomplished on the mixture of CNT and chitosan and then, nano magnetite was added. Preparation of catalyst C was the same as A with the substitution of PVA for chitosan as gelation agent. In catalyst D, nano magnetite was prepared in in-situ way on CNT and then gelation was performed using chitosan. As we will see in Table 1 and next pages, catalyst D was shown the highest catalytic activity, therefore, all analyses except FESEM images) were performed only on this selected catalyst, as will be stated in the next paragraphs.

The schematic presentation of the preparation of catalyst D is presented in Figure 1 and the details of its preparation are mentioned in the method section. The major structural and functional group analyses of this catalyst and its ingredients, including XRD patterns, FTIR spectra, Raman spectrum, and VSM analyses, are shown in Figure 1.

The XRD patterns of the CNT aerogel, Fe_3O_4 nanoparticles, and catalyst D (Figure 2-top left) show the characteristic structural features of each component. In both CNT-containing samples, a broad diffraction peak at approximately 2θ = 25.9° was observed, corresponding to the (002) plane of graphitic carbon[35], indicating that the graphitic structure of CNTs was preserved after aerogel formation and magnetite incorporation. A broad peak centered at approximately 2θ ≈ 20°, attributed to the amorphous structure of chitosan[36], was more pronounced in the Fe_3O_4/CNT aerogel than in the CNT aerogel, indicating enhanced interactions among chitosan, CNTs, and Fe_3O_4 nanoparticles within the hybrid network. Both Fe_3O_4 and Fe_3O_4/CNT aerogels exhibited characteristic diffraction peaks at 2θ values of 30.2°, 35.7°, 43.1°, 53.7°, 57.0°, and 62.6°, corresponding to the (220), (311), (400), (422), (511), and (440) planes of spinel Fe_3O_4 [37], confirming the successful incorporation of magnetite without phase transformation. The reduced intensity of these peaks in the composite sample can be attributed to the lower relative content of Fe_3O_4, its homogeneous dispersion within the aerogel matrix, and its interactions with chitosan and CNTs. The absence of additional diffraction peaks suggests that no crystalline impurities were formed during synthesis. The average crystallite sizes of the Fe_3O_4 and Fe_3O_4/CNT aerogels, calculated using the Scherrer equation [38], were 14.28 ± 0.72 nm and 9.73 ± 2.16 nm, respectively. The decrease in crystallite size after incorporation into the CNT/chitosan aerogel may be attributed to the confinement effect of the porous matrix and interactions between the Fe species and functional groups of chitosan and CNT-COOH, which limit particle growth and aggregation.

The FTIR spectra of the pristine aerogel, magnetic aerogel, and Fe_3O_4 nanoparticles are shown in Figure 2 (top right). The characteristic absorption bands observed at 580 and 634 cm^{-1} for the Fe_3O_4 nanoparticles were assigned to the Fe–O stretching vibrations [39]. After incorporation into the aerogel matrix, these bands shifted to 588 and 646 cm^{-1}, respectively. The shift toward higher wavenumbers suggests modifications in the local chemical environment of the Fe–O bonds, likely arising from

interactions between the Fe_3O_4 nanoparticles and the aerogel framework. These interactions may involve the carboxyl groups of the functionalized carbon nanotubes and hydrogen bonding between chitosan and carbon nanotubes. Further evidence for these interactions is provided by the broadening and increased intensity of the absorption band centered at 3437 cm^{-1}, corresponding to the stretching vibrations of the O–H and N–H groups. This observation suggests the participation of hydroxyl and amino functionalities in the stabilization of Fe_3O_4 nanoparticles within the aerogel structure. The absorption bands located at 1087 cm^{-1} for the pristine aerogel and 1089 cm^{-1} for the magnetic aerogel are attributed to the C–O and C–O–C stretching vibrations of chitosan. In the 1600–1500 cm^{-1} region, the single band observed at 1568 cm^{-1} in the pristine aerogel split into two bands at 1633 and 1537 cm^{-1} after magnetic modification, indicating significant changes in the local chemical environment of amino-related groups owing to strong interfacial interactions within the composite structure. Supporting this interpretation, the carbonyl stretching vibration associated with the carboxylic acid groups of the functionalized carbon nanotubes shifted from 1708 cm^{-1} in the pristine aerogel to 1695 cm^{-1} in the magnetic aerogel, indicating the involvement of carboxyl groups in the interfacial interactions within the composite structure. Furthermore, the bands located at approximately 1407 and 1402 cm^{-1} in the FTIR spectra of the pristine and magnetic aerogels, respectively, are attributed to the CH_2 bending vibrations of the chitosan backbone. The absorption bands at 2854 and 2923 cm^{-1} correspond to the symmetric and asymmetric C–H stretching vibrations of the CH_2 and CH_3 groups, respectively. The preservation of these characteristic bands demonstrates that the fundamental structure of chitosan remained intact after incorporating Fe_3O_4 nanoparticles. Overall, the FTIR results confirm the successful integration of Fe_3O_4 nanoparticles into the aerogel matrix and reveal the presence of interfacial interactions among chitosan, functionalized carbon nanotubes, and Fe_3O_4 nanoparticles, which contribute to the structural integrity and stability of the magnetic aerogel. [40,41]

To further elucidate the structural characteristics of the catalyst and embedded carbon framework, Raman spectroscopy was performed. As illustrated in the Raman spectrum of catalyst D in Fig 2 (bottom left). three characteristic bands at 1337.68, 1569, and 2684.27 cm^{-1}, which are assigned to the D, G, and 2D (G') bands of multi-walled carbon nanotubes (MWCNTs), are clearly observed, respectively. These features fall within the typical Raman ranges of graphitic carbon materials (~1300–1350 cm^{-1} for the D band, ~1580–1600 cm^{-1} for the G band, and ~2600–2700 cm^{-1} for the 2D band), confirming the preservation of the sp^2 carbon network after composite formation. The D band is associated with defect-induced vibrational modes in sp^2 carbon, whereas the G band corresponds to the in-plane stretching of graphitic domains. The presence of a well-defined 2D band further supports the retention of graphitic order in the MWCNT structure. The increase in the I_D/I_G ratio from 0.80 for pristine CNTs to 0.85 for the magnetic aerogel indicates the generation of additional structural defects and disorder within the carbon framework. This increase can be attributed to the formation of interfacial interactions and chemical bonding between the CNT network and the magnetic Fe_3O_4 phase during aerogel fabrication, confirming the successful integration of the components. A weak band observed at 3199.79 cm^{-1} can be attributed to overtone or combination modes commonly reported in graphitic carbon systems. Minor variations in the Raman band positions (10–13 cm^{-1}) compared with the reference MWCNT values may be related to

the measurement conditions and subtle changes in the local chemical environment. Overall, the Raman results are consistent with FTIR and XRD analyses, collectively supporting the preservation of the graphitic structure and indicating possible interfacial interactions within the composite system. [42–44]

VSM measurements (Figure 2, bottom right) were performed to evaluate the magnetic properties of the synthesized Fe_3O_4 nanoparticles and magnetic aerogels. The Fe_3O_4 nanoparticles exhibited a saturation magnetization of approximately 67 emu g^{-1}, whereas the magnetic aerogel showed a lower value of 6.68 emu g^{-1}. This decrease can be attributed to the incorporation of nonmagnetic organic components within the aerogel framework, the coating of Fe_3O_4 nanoparticles by chitosan and carbon nanotubes, and the reduction in Fe_3O_4 crystallite size after immobilization in the aerogel matrix, as evidenced by the XRD results [45]. These factors increase the contribution of surface spin disorder and reduce the overall magnetic response of the composite. Nevertheless, the magnetic aerogel retained sufficient magnetic responsiveness for rapid recovery using an external magnet. Furthermore, both samples exhibited negligible coercivity (Hc ≈ 0) and remanent magnetization (Mr ≈ 0), confirming their superparamagnetic behavior. Such characteristics are advantageous for catalytic applications, enabling facile magnetic separation and catalyst reuse.

Representative SEM micrographs of catalysts A–D, as well as the elemental mapping and EDS analysis of catalyst D are presented in Figure 3. SEM analysis revealed significant differences in the morphology and structural organization of the synthesized samples between the two groups. Sample A exhibited a less integrated carbon nanotube network. The nanotubes appeared loosely arranged with weaker interconnections than the reference catalyst (Sample D). However, the Fe_3O_4 nanoparticles were more uniformly distributed and exhibited lower levels of aggregation, which may be attributed to the lower Fe_3O_4 content used in this sample. For Sample B, the nanoparticles were predominantly located on the external surface of the framework. In contrast to Sample D, the carbon nanotube network exhibited reduced structural cohesion and fewer interconnections between the nanotubes. Moreover, localized nanoparticle agglomeration was observed in several regions. Sample C, containing poly(vinyl alcohol) as a crosslinking agent, displayed an integrated 3D network with good structural cohesion. Nevertheless, the Fe_3O_4 nanoparticles exhibited a higher degree of aggregation than the other samples, indicating that the presence of PVA did not effectively inhibit nanoparticle agglomeration. Among the investigated samples, Sample D exhibited the most homogeneous morphology and the highest degree of structural integration. The carbon nanotubes formed a continuous interconnected network, while the Fe_3O_4 nanoparticles were distributed throughout the framework with relatively limited aggregation that EDS analysis confirmed by the EDS analysis, which are shown in Figure 3 (E-I). All elemental mapping images (3E-H) show the uniform distribution of the integrated elements. These observations suggest that the synthesis strategy employed for Sample D promoted both network formation and nanoparticle incorporation into the aerogel structure. Moreover, the elemental percents, presented by EDS analysis, are in appropriate agreement with the used values in the experiment, considering this fact that EDS is the surface analysis and not a complete atomic analysis.

N_2 adsorption–desorption analysis was performed and their results are shown in Figure 4 (a-d). The isotherm diagram (4a) revealed a Type IV isotherm with an H1 hysteresis loop, confirming a mesoporous structure. The BET surface area was 8.2 $m^2 g^{-1}$, with a pore volume of 0.0746 $cm^3 g^{-1}$ and an average pore diameter of 18.159 nm. BJH analysis indicated a dominant mesopore population around ~18 nm with minor contributions from smaller pores (<10 nm). T-plot results suggested negligible microporosity, whereas DA analysis confirmed a limited micropore volume (0.123 $cm^3 g^{-1}$). Overall, the material exhibits a predominantly mesoporous hierarchical structure consistent with SEM observations.

TGA and DTG analyses, where are shown in Figure 4e, revealed a two-step weight loss profile. The initial loss at 57°C–70°C is attributed to the removal of adsorbed water inherent to the hydrophilic nature of chitosan, whereas the major loss (~20%) at ~256 °C corresponds to chitosan thermal decomposition via chain scission and functional group degradation. This two-step mass loss confirms the typical thermal behavior of chitosan within the composite. Above this region, the material maintains high thermal stability up to 500 °C due to the reinforcing effect of CNTs and Fe_3O_4 through strong interfacial interactions. Overall, the composite exhibits suitable thermal stability and small weight loss for catalytic applications within the reaction temperature range. [46–48]

The wettability of the prepared aerogels was evaluated using the sessile drop method with deionized water and isopropanol as probe liquids. A droplet of approximately 4 µL was deposited onto the surface using a microsyringe, and side-view images were acquired immediately after deposition. According to the obtained images, which are shown in Figure S1 (at supporting information), apparent contact angles were determined using ImageJ software. The CNT-based aerogel exhibited a water contact angle of 58.3°, indicating a moderately hydrophilic surface. The droplet progressively infiltrated the porous structure and was completely absorbed within ~1 min. In contrast, the magnetic aerogel showed a lower contact angle of 47.5° and a markedly faster absorption time (~4 s), suggesting enhanced wettability. This improvement in hydrophilicity can be attributed to the incorporation of Fe_3O_4 nanoparticles and the highly interconnected porous network, which promote liquid infiltration and interfacial interactions. In contrast, isopropanol droplets were rapidly absorbed by both aerogels, preventing reliable determination of contact angles. This behavior is attributed to the low surface tension of isopropanol and the highly porous nature of the aerogel structure. Such wettability differences are likely to influence mass transfer behavior and interfacial accessibility within the porous network, which are critical factors governing the adsorption and catalytic efficiency aerogels.

Catalyst activity experiments

After the successful preparation of all four catalysts, a model reaction was designed to examine their catalytic abilities. This model includes 1 mmol of nitrobenzene, 5 mL 2-propanol (as both solvent and reducing agent), 20 mg catalyst, 3 mmol NaOH at reflux condition (~ 83 °C, the boiling point of 2-propanol) in 24 h. The model reaction was employed basically for the optimization of the reaction conditions. The yields of the optimization reactions were obtained using the major aniline (as a product) absorption at 232 nm. The standard diagram (shown in Figure S2) was obtained from the standard

aniline solutions with different concentrations and the amount of aniline in each reaction (and so the reaction yield) was obtained by connecting the observed absorption to the concentration in the standard diagram.

The UV–Vis absorption profiles of the reaction mixtures obtained in the presence of bare Fe_3O_4, the CNT aerogel, and the magnetically integrated CNT–Fe_3O_4–chitosan aerogels (catalysts A-D), shown in Figure 4f, exhibit similar overall spectral evolution, with discernible differences in the relative intensity of the band associated with intermediate species. In all systems, the absorption features around ~232 nm, is consistent with formation of the aniline, while the band centered at ~322 nm has less importance because of the smaller strength and possibility of overlap with nitrobenzene and other intermediates absorptions. A comparison between bare Fe_3O_4 and Sample D shows comparable conversion behavior based on the ~232 nm signal. However, Sample D exhibits a more evident decrease in the ~322 nm band intensity, indicating a lower accumulation of intermediate-related species under identical reaction conditions.

Quantitative results, related to the optimization experiments (Table 1, entries 1-6), further confirm that Sample D and bare Fe_3O_4 provide similar conversion efficiencies (72% and 69%, respectively), whereas the CNT aerogel shows lower conversion (37%). Among Samples A–C, the observed variation in conversion (49%, 45%, and 11%) highlights the influence of composition and preparation route on catalytic performance. Overall, the spectral trends suggest that the magnetically integrated aerogel system influences the reaction profile, particularly in terms of intermediate-associated absorption features.

In the next experiments, optimization of the other reaction conditions was performed on the model reaction using catalysts D. The effects of catalyst loading, temperature, NaOH amount, and reaction time were systematically evaluated, and the results are summarized in the next rows of Table 1. Moreover, their related UV-Vis spectra were depicted at figures S3-S6, at supporting information. The catalyst loading was first examined by running the model reaction with varying amounts. Yield increased up to 20 mg, likely due to a greater availability of accessible active sites. A further increase in catalyst loading led to lower yields, possibly because of side reactions or reduced accessibility of active sites. The effect of temperature was then studied using the optimized catalyst loading. Raising the temperature enhanced conversion, and the highest yield was obtained under reflux conditions (83 °C). This behavior can be attributed to more efficient dehydrogenation of 2-propanol, which in turn provides greater availability of active hydrogen species required for nitro group reduction. Next, the amount of NaOH was varied from 1 to 4 equivalents. In the absence of sufficient base, the generation of hydrogen from 2-propanol is limited, resulting in lower conversions. Among the investigated values, 3 equivalents of NaOH afforded the most favorable reaction outcome. Higher NaOH loadings resulted in lower yields, which may be related to increased viscosity of the reaction medium and less efficient mass transfer. Finally, the reaction time was evaluated under the selected conditions. The conversion increased during the first 6 h, decreased between 6 and 18 h, and then increased again to reach its maximum after 24 h. Accordingly, 24 h was selected as the reaction time for subsequent studies. Therefore, subsequent reactions were conducted

using 20 mg of catalyst and 3 equivalents of NaOH in 5 mL of 2-propanol under reflux and a nitrogen atmosphere for 24 h. **Catalytic reduction of other nitrobenzene derivatives**

To evaluate the performance and versatility of the catalyst in the reduction of nitrobenzene derivatives, 24 substrates were examined under optimized conditions. The conversion and yield were determined by UV–Vis spectroscopy, TLC analysis, and gravimetric measurements. The results are summarized in Table 2. The influence of electron-donating substituents such as amino and methyl groups in positions relative to the nitro group was investigated. In general, meta-substituted derivatives showed slightly higher performance than the corresponding para isomers. For nitrobenzaldehyde derivatives, the ortho isomer showed a higher yield than the para isomer, whereas the para isomer performed better than the meta isomer, indicating a position-dependent effect on the reaction outcome. Halogen-substituted substrates showed good reactivities. In particular, 4-bromonitrobenzene afforded 90 % yield, although full conversion was not achieved. In contrast, substrates containing strongly deactivating groups such as additional nitro substituents showed conversion. Similarly, 4-nitrophenol was unreactive under the reaction conditions.

Reusability of the catalyst

The reusability of the magnetic catalyst was evaluated over four consecutive cycles. After each run, the catalyst was magnetically separated, washed with deionized water and ethanol, and dried at room temperature before reuse. As shown in Figure 5a, a 13% decrease in activity was observed after the first cycle, whereas no further significant loss occurred in subsequent cycles. Moreover, after these fur runs, post-reaction characterization of the catalyst was performed using FTIR, XRD, and VSM. VSM analysis (Figure 5b) showed only a little decrease in the magnetic properties, probably because of the leaching of nano magnetite particles. The FTIR spectrum of the recovered catalyst in Figure 5c showed no noticeable changes compared with the fresh sample, with characteristic bands at ~3300 cm^{-1}, 1535 cm^{-1}, 1093 cm^{-1}, and 657 cm^{-1} attributed to O–H/N–H, C–N, C–O, and Fe–O vibrations, respectively. XRD patterns (Figure 5d) retained the characteristic reflections of Fe_3O_4 at 2θ = 30.5°, 35.75°, 43.4°, 57.2°, and 63°, confirming the preservation on of the crystalline phase. Additional peaks at 2θ = 26.5° and 20.4° were assigned to carbon nanotubes and chitosan, respectively, with no significant changes after reuse. Overall, FTIR, XRD, and VSM results confirm that the catalyst retains its structural, phase, and magnetic properties after repeated cycles.

Comparison with previous studies

The advancement of efficient and sustainable catalytic systems for the reduction of nitroarenes remains a significant focus in both academic and industrial research. Consequently, a multitude of catalytic protocols have been documented for this transformation under diverse reaction conditions. The variation in reaction conditions and catalyst types across these protocols complicates the precise comparison of their catalytic efficiencies. Nonetheless, the data presented in Table 3 indicate that certain methodologies require the use of noble-metal-based catalysts or harsh reaction conditions, such as elevated temperatures and pressures, which reduce their attractiveness from both economic and

environmental perspectives. Furthermore, the synthesis of some catalytic systems demands expensive raw materials and involves multistep preparation processes, thereby diminishing their economic viability. In contrast, the Fe_3O_4–CNT aerogel was synthesized through a straightforward procedure utilizing inexpensive and readily available materials., effectively promoting the reduction reaction under relatively mild conditions without the need for noble metals. Moreover, its magnetic nature enables facile separation and recovery from the reaction medium. Therefore, Fe_3O_4–CNT aerogels can be considered promising, cost-effective, and environmentally friendly catalysts with catalytic performance comparable to that of several previously reported catalytic systems.

Methods

Materials and instruments

The morphology and microstructure of the prepared materials were investigated using field-emission scanning electron microscopy (FESEM, QUANTA FEG-450, FEI, USA). Fourier-transform infrared (FTIR) spectra were recorded using a Tensor 27 spectrometer (Bruker, Germany) in the range of 400–4000 cm^{-1}. Raman spectroscopy was performed using a LabRAM HR Raman spectrometer (Horiba, Japan) with a 532-nm excitation laser. X-ray diffraction patterns were recorded using an Asenware AW-XDM300 diffractometer equipped with Cu Kα radiation (λ = 1.5406 Å). The diffraction data were collected to determine the crystalline structure and phase composition of the samples. Measurements were performed over a 2θ range of 10°–80° with a step size of 0.05° and a step time of 1 s to identify the characteristic diffraction peaks. Thermal stability was evaluated by thermogravimetric analysis (TGA) using a Labsys Evo thermal analyzer (Setaram, France) under an argon atmosphere over a temperature range of 25°C–800°C at a heating rate of 10°C min^{-1}. Magnetic properties were measured using a vibrating sample magnetometer (VSM, MDKB, Maghnatis Danesh Pajouh Co., Tehran, Iran). Specific surface area and pore characteristics were determined from nitrogen adsorption–desorption isotherms using a BELSORP surface area analyzer (MicrotracBEL, Japan), and the surface area was calculated based on the Brunauer–Emmett–Teller method. UV–Vis spectroscopy and catalytic activity measurements were performed using a V-570 UV–Vis spectrophotometer (JASCO, Japan).

Carboxyl-functionalized multi-walled carbon nanotubes (MWCNT-COOH, > 99% purity) were procured from US Research Nanomaterials, Inc. Chitosan, with a medium molecular weight, was sourced from Sigma-Aldrich. Ferric chloride hexahydrate (FeCl3·6H2O, 99%), ferrous chloride tetrahydrate (FeCl2·4H2O, 99%), sodium hydroxide (NaOH, 99%), glacial acetic acid (CH3COOH, 99%), 2-propanol (99%), and poly(vinyl alcohol) (PVA, Mw ≈ 145,000) were acquired from Merck. The study used aqueous ammonia solution (25 wt%) and deionized water. All chemicals were employed as received, without additional purification, unless specified otherwise.

Chitosan deacetylation

Before application, chitosan underwent additional deacetylation. Specifically, 3 g of chitosan was subjected to treatment with a 50 wt% NaOH solution (50 mL) at 110°C for a duration of 2 hours, with continuous stirring. The resultant solid was subsequently collected via filtration, thoroughly washed with deionized water, and dried overnight.

Synthesis of Fe_3O_4 nanoparticles

$FeCl_3 \cdot 6H_2O$ (5 mmol) and $FeCl_2 \cdot 4H_2O$ (2.5 mmol) were dissolved in deionized water (50 mL) and sonicated for 30 min. Aqueous ammonia (25%) was added dropwise via syringe until pH 9–10, upon which the solution turned dark black, indicating Fe_3O_4 formation. The mixture was stirred under N_2 at 80°C for 1 h. The resulting nanoparticles were collected with a strong magnet, washed twice with ethanol, and dried at 80°C for 12 h.

Synthesis of magnetic CNT aerogels

Four different aerogel composites were prepared using four different ways from carboxylated multi-walled carbon nanotubes. Samples A, B, and C differ in the stage at which magnetite is incorporated into the composite; in samples A and B, the Fe_3O_4:MWCNT mass ratio was 1:2 and the chitosan:MWCNT ratio was 5:1. In Sample D, the Fe_3O_4:MWCNT mass ratio was 5:1 and the chitosan:MWCNT ratio was 5:1. Sample C substituted poly(vinyl alcohol) (PVA) instead of chitosan as the crosslinking polymer while maintaining the same Fe_3O_4:MWCNT ratio.

Sample A. Pre-synthesized Fe_3O_4 (0.1 g) and carboxylated MWCNTs (0.2 g) were dispersed in deionized water (100 mL) by sonication (45 min). Chitosan (1 g) was added in portions under stirring at room temperature (2 h). The mixture was heated at 80°C until the volume was halved. After cooling to room temperature, glacial acetic acid (several drops) was added to induce gelation. The gel was transferred to a glass Petri dish (d = 5 cm, depth = 1.5 cm), frozen at − 18°C (48 h), and freeze-dried (24 h).

Sample B. Carboxylated MWCNTs (0.2 g) were dispersed in deionized water (90 mL) by sonication (45 min). Chitosan (1 g) was added in portions under stirring (room temperature, 2 h), and the mixture was heated at 80°C to halve the volume. After cooling, glacial acetic acid (several drops) was added to form a gel. Pre-synthesized Fe_3O_4 (0.05 g) pre-dispersed in deionized water (5 mL) by sonication (30 min) was then mixed into the pre-formed gel. The mixture was transferred to a glass Petri dish (d = 5 cm, depth = 2 cm), frozen at − 18°C (48 h), and freeze-dried (24 h).

Sample C. Pre-synthesized Fe_3O_4 (0.1 g) and carboxylated MWCNTs (0.2 g) were dispersed in deionized water (75 mL) by sonication (45 min). A 1% (w/v) PVA solution (25 mL) was added in portions under stirring, followed by sonication (1 h). The volume was reduced by half at 80°C. Upon cooling to room temperature, a homogeneous, low-viscosity gel was obtained without phase separation. The gel was transferred to a glass Petri dish, frozen at − 18°C (48 h), and freeze-dried (24 h).

Sample D. $FeCl_3 \cdot 6H_2O$ (1 g, 3.7 mmol) and carboxylated MWCNTs (0.2 g) were added to deionized water (150 mL) and sonicated (1 h). $FeCl_2 \cdot 4H_2O$ (0.35 g, 1.76 mmol) was added under stirring, and the mixture was heated to 80°C under N_2 (30 min. Aqueous ammonia (25%, ~ 25 mL) was added dropwise via a syringe until pH 10, and the reaction was stirred for 2 h. The Fe_3O_4-decorated MWCNTs were collected with a strong magnet, washed three times with deionized water, and dried at room temperature. The product was re-dispersed in deionized water (100 mL) by sonication (45 min). Chitosan (1 g) was added under stirring (room temperature, 2 h), and the mixture was heated at 80°C until the volume was halved. After cooling, glacial acetic acid (3 drops) was added to form a homogeneous gel. The gel was transferred to a glass Petri dish (d = 5 cm, depth = 2 cm), frozen at − 18°C (48 h), and freeze-dried (24 h).

The hydrogenation of nitroarenes

For the reduction of nitrobenzene, nitrobenzene (1 mmol, 102 µL) was added to a 25 mL round-bottom flask containing isopropanol (5 mL) as the hydrogen donor. Subsequently, NaOH (3 mmol, 120 mg) and CNT–Fe_3O_4 magnetic aerogel catalyst (20 mg) was added to the reaction mixture. The flask was equipped with a condenser, purged with nitrogen, and the reaction was conducted under a nitrogen atmosphere at 82°C under reflux with continuous stirring. The reaction progress was monitored by thin-layer chromatography (TLC). Upon completion, the catalyst was separated magnetically using an external magnet. The reaction mixture was then appropriately diluted, and the conversion of nitrobenzene was determined by UV–Vis spectroscopy using a previously established calibration curve. By diluting the obtained reaction product to an approximate concentration of 50 µM, the amount of aniline (AN) produced was determined.

Conclusion

This study successfully synthesized a magnetic CNT–Fe_3O_4 aerogel catalyst, which was subsequently applied to the transfer hydrogenation of nitrobenzene and various nitroarene derivatives under mild reaction conditions. Comprehensive physicochemical characterization, including FTIR, XRD, BET, Raman, VSM, TGA, and FESEM, confirmed the formation of a porous magnetic aerogel with well-defined structural, thermal, and magnetic properties. The catalytic performance was evaluated using isopropanol as a hydrogen donor under a nitrogen atmosphere at 83°C in the presence of a base. Under optimized conditions, nitrobenzene was efficiently reduced to aniline with a yield of 72%. Additionally, the catalyst demonstrated a broad substrate scope, effectively reducing 24 nitroarene derivatives with generally good yields, including efficient performance for halogen-substituted substrates. The catalyst was readily recovered by magnetic separation and reused for four consecutive cycles with only a slight loss of activity, indicating its good stability and recyclability. Finally, the use of an inexpensive hydrogen source, mild reaction conditions, facile magnetic separation, and satisfactory catalytic efficiency highlights the potential of CNT–Fe_3O_4 aerogels as sustainable and reusable catalysts for transfer hydrogenation reactions.

Declarations

Competing interests

The authors declare no competing interests.

Additional information

Supplementary Information The online version contains supplementary material available at

Correspondence and requests for materials should be addressed to H.T.

Funding statement

This work is based upon research funded by Iran National Science Foundation (INSF) under project No. 4038346.

Author Contribution

A.A. performed the investigation and wrote the manuscript draft. H.T. designed and supervised the work, provide facilities, and corrected and sent the manuscript.

Acknowledgement

We are acknowlege the research affair of Isfahan University of Technology, because of the partial support of this work.

Data Availability

All data generated or analyzed during this study are included in this published article and its supplementary information files.

References

1. Kadam, H. K. & Tilve, S. G. Advancement in methodologies for reduction of nitroarenes. *RSC Adv.* **5**, 83391–83407. https://doi.org/10.1039/C5RA10076C (2015).
2. Guo, W., Zheng, Y., Xiang, W. & Zhang, Y. Advances in the catalysis of reduction of nitroaromatics and its mechanism: a tutorial review. *RSC Sustain.* **3**, 243–254. https://doi.org/10.1039/D4SU00531G (2025).
3. Patel, A. R., Patel, I. & Banerjee, S. Importance and green synthesis of amines: A Review. *COC* **28**, 375–389. https://doi.org/10.2174/0113852728296565240221082253 (2024).

4. Penning, T. M., Su, A. L., El-Bayoumy, K. & Nitroreduction A critical metabolic pathway for drugs, environmental pollutants, and explosives. *Chem. Res. Toxicol.* **35**, 1747–1765. https://doi.org/10.1021/acs.chemrestox.2c00175 (2022).
5. Song, J. et al. Review on selective hydrogenation of nitroarene by catalytic, photocatalytic and electrocatalytic reactions. *Appl. Catal. B*. **227**, 386–408. https://doi.org/10.1016/j.apcatb.2018.01.052 (2018).
6. Liu, M., Song, X., Xu, K., Wei, Z. & Xie, K. Recent advances in catalysts for selective hydrogenation of nitro compound. *Int. J. Hydrogen Energy*. **128**, 22–46. https://doi.org/10.1016/j.ijhydene.2025.04.195 (2025).
7. Taleb, B. et al. Exploring hydrogen sources in catalytic transfer hydrogenation: a review of unsaturated compound reduction. *Molecules* **28**, 7541. https://doi.org/10.3390/molecules28227541 (2023).
8. Wang, C., Li, J., Zhang, F., Zhao, Y. & Xiao, T. Heterogeneous synergistic catalysts enable efficient catalytic transfer hydrogenation of nitro compounds via in-situ provided hydrogen. *Int. J. Hydrogen Energy*. **51**, 1286–1305. https://doi.org/10.1016/j.ijhydene.2023.11.076 (2024).
9. Wang, X., Liang, M., Zhang, J. & Wang, Y. Selective hydrogenation of aromatic chloronitro compounds. *COC* **11**, 299–314. https://doi.org/10.2174/138527207779940856 (2007).
10. Trincado, M., Banerjee, D. & Grützmacher, H. Molecular catalysts for hydrogen production from alcohols. *Energy Environ. Sci.* **7**, 2464–2503. https://doi.org/10.1039/C4EE00389F (2014).
11. Wang, D., Deraedt, C., Ruiz, J. & Astruc, D. Sodium hydroxide-catalyzed transfer hydrogenation of carbonyl compounds and nitroarenes using ethanol or isopropanol as both solvent and hydrogen donor. *J. Mol. Catal. A: Chem.* **400**, 14–21. https://doi.org/10.1016/j.molcata.2015.01.024 (2015).
12. Chen, S., Lu, G. & Cai, C. Iridium-catalyzed transfer hydrogenation of nitroarenes to anilines. *New. J. Chem.* **39**, 5360–5365. https://doi.org/10.1039/C5NJ00917K (2015).
13. Das, V. K. et al. Graphene derivative in magnetically recoverable catalyst determines catalytic properties in transfer hydrogenation of nitroarenes to anilines with 2-Propanol. *ACS Appl. Mater. Interfaces*. **10**, 21356–21364. https://doi.org/10.1021/acsami.8b06378 (2018).
14. Moran, M. J. et al. Tuneable copper catalysed transfer hydrogenation of nitrobenzenes to aniline or azo derivatives. *Adv. Synth. Catal.* **362**, 2689–2700. https://doi.org/10.1002/adsc.202000127 (2020).
15. Payamifar, S., Foroozandeh, A. & Abdouss, M. Poursattar Marjani, A. magnetic nickel nanoparticle catalyst on β-cyclodextrin-modified Fe_3O_4 for nitroarene hydrogenation. *Sci. Rep.* **14**, 28493. https://doi.org/10.1038/s41598-024-79709-0 (2024).
16. Niculescu, A. G., Chircov, C. & Grumezescu, A. M. Magnetite nanoparticles: synthesis methods–a comparative review. *Methods* **199**, 16–27. https://doi.org/10.1016/j.ymeth.2021.04.018 (2022).
17. Gawande, M. B., Branco, P. S. & Varma, R. S. Nano-magnetite (Fe_3O_4) as a support for recyclable catalysts in the development of sustainable methodologies. *Chem. Soc. Rev.* **42**, 3371–3393. https://doi.org/10.1039/C3CS35480F (2013).

18. Zhou, D., Zhou, Y., Li, Y. & Shen, W. Nanostructured iron oxides for heterogeneous catalysis. *J. Energy Chem.* **6**, 100124. https://doi.org/10.1016/j.enchem.2024.100124 (2024).
19. Chishti, A. N. et al. Preparation of novel magnetic noble metals supramolecular composite for the reduction of organic dyes and nitro aromatics. *Chin. Chem. Lett.* **34**, 108122. https://doi.org/10.1016/j.cclet.2022.108122 (2023).
20. Zhang, Q., Yu, L., Liu, B., Li, F. & Tang, B. Reduction of nitroarenes by magnetically recoverable nitroreductase immobilized on Fe_3O_4 nanoparticles. *Sci. Rep.* **10**, 2810. https://doi.org/10.1038/s41598-020-59754-1 (2020).
21. Gholidizchi, L. A., Ebrahimkhas, M. & Hooshyar, H. GO@ CNT@ Fe_3O_4@ CuO quaternary nanohybrids enhance dielectric-magnetic synergy for high-performance epoxy-based electromagnetic absorbers. *Sci. Rep.* **16**, 8927. https://doi.org/10.1038/s41598-026-41828-1 (2026).
22. Göksu, H., Zengin, N., Burhan, H., Cellat, K. & Şen, F. A novel hydrogenation of nitroarene compounds with multi wall carbon nanotube supported palladium/copper nanoparticles (PdCu@ MWCNT NPs) in aqueous medium. *Sci. Rep.* **10**, 8043. https://doi.org/10.1038/s41598-020-64988-0 (2020).
23. Barrios, E. et al. Nanomaterials in advanced, high-performance aerogel composites: a review. *polymers* 11, 726; (2019). https://doi.org/10.3390/polym11040726
24. Kohlmeyer, R. R., Lor, M., Deng, J., Liu, H. & Chen, J. Preparation of stable carbon nanotube aerogels with high electrical conductivity and porosity. *Carbon* **49**, 2352–2361. https://doi.org/10.1016/j.carbon.2011.02.001 (2011).
25. Guo, J. et al. Recent advances in magnetic carbon nanotubes: synthesis, challenges and highlighted applications. *J. Mater. Chem. B*. **9**, 9076–9099. https://doi.org/10.1039/D1TB01242H (2021).
26. Zou, J. et al. Ultralight multiwalled carbon nanotube aerogel. *ACS nano*. **4**, 7293–7302. https://doi.org/10.1021/nn102246a (2010).
27. Goncalves, J. O. et al. Chitosan hydrogel scaffold modified with carbon nanotubes and its application for food dyes removal in single and binary aqueous systems. *Int. J. Biol. Macromol.* **142**, 85–93. https://doi.org/10.1016/j.ijbiomac.2019.09.074 (2020).
28. Ali, D. A. & Ali, R. G. Green synthesis of carbonized chitosan-Fe_3O_4-SiO_2 nano-composite for adsorption of heavy metals from aqueous solutions. *BMC Chem.* **18**, 147. https://doi.org/10.1186/s13065-024-01257-5 (2024).
29. Shen, Y., Zheng, Q., Liu, J. & Tu, T. Metallo-aerogels derived from chitosan with encapsulated metal nanoparticles as robust, efficient and selective nanocatalysts towards reduction of nitroarenes. *Nano Res.* **14**, 59–65. https://doi.org/10.1007/s12274-020-3040-1 (2021).
30. Lv, S. et al. Progress in preparation and properties of chitosan-based hydrogels. *Int. J. Biol. Macromol.* **242**, 124915. https://doi.org/10.1016/j.ijbiomac.2023.124915 (2023).
31. Carson, L. et al. Synthesis and characterization of chitosan–carbon nanotube composites. Mater. Lett. 63, 617–620 ; (2009). https://doi.org/10.1016/j.matlet.2008.11.060

32. Yousefian-Jazi, Z. & Tavakol, H. Using isopropanol as a Liquid Organic Hydrogen Carrier (LOHC) for the Reduction Nitroarenes Employing Au/Ag Decorated Carbon Aerogels. *J. Ind. Chem. Soc.* **102116** https://doi.org/10.1016/j.jics.2025.102116 (2025).
33. Tavakol, H. & Tarkesh, H. Synthesis, characterization, and catalytic application of biocompatible chitosan-graphene oxide aerogel in the retro-aza-Henry-type conversion. *J. Ind. Chem. Soc.* **102**, 101875. https://doi.org/10.1016/j.jics.2025.101875 (2025).
34. Sadegh, F. & Tavakol, H. Synthesis of Ag/CoFe2O4 magnetic aerogel for catalytic reduction of nitroaromatics. *Results Chem.* **4**, 100592. https://doi.org/10.1016/j.rechem.2022.100592 (2022).
35. Dang, A. et al. High-efficient adsorption for versatile adsorbates by elastic reduced graphene oxide/Fe_3O_4 magnetic aerogels mediated by carbon nanotubes. *J. Hazard. Mater.* **457**, 131846. https://doi.org/10.1016/j.jhazmat.2023.131846 (2023).
36. Zhang, S., Feng, J., Feng, J., Jiang, Y. & Li, L. Ultra-low shrinkage chitosan aerogels trussed with polyvinyl alcohol. *Mater. Des.* **156**, 398–406. https://doi.org/10.1016/j.matdes.2018.07.004 (2018).
37. Ge, J., Hu, Y., Biasini, M., Beyermann, W. P. & Yin, Y. Superparamagnetic magnetite colloidal nanocrystal clusters. *Angew Chem. Int. Ed.* **46**, 4342–4345. https://doi.org/10.1002/anie.200700197 (2007).
38. Holzwarth, U. & Gibson, N. The Scherrer equation versus the'Debye-Scherrer equation'. *Nat. Nanotechnol*. **6**, 534–534. https://doi.org/10.1038/nnano.2011.145 (2011).
39. Xuan, S., Wang, F., Wang, Y. X. J., Yu, J. C. & Leung, K. C.-F. Facile synthesis of size-controllable monodispersed ferrite nanospheres. *J. Mater. Chem.* **20**, 5086–5094. https://doi.org/10.1039/C0JM00159G (2010).
40. Tabatabaei Rezaei, S. J. et al. Chemoselective reduction of nitro and nitrile compounds with magnetic carbon nanotubes-supported Pt(II) catalyst under mild conditions. *Ind. Eng. Chem. Res.* **56**, 12256–12266. https://doi.org/10.1021/acs.iecr.7b02795 (2017).
41. Chang, X., Chen, D. & Jiao, X. Chitosan-based aerogels with high adsorption performance. *J. Phys. Chem. B*. **112**, 7721–7725. https://doi.org/10.1021/jp8011359 (2008).
42. Jorio, A. & Saito Rjj. Raman spectroscopy for carbon nanotube applications. *J. Appl. Phys.* **129**, 021102. https://doi.org/10.1063/5.0030809 (2021).
43. Dresselhaus, M. S., Dresselhaus, G., Saito, R. & Jorio, A. Raman spectroscopy of carbon nanotubes. *Phys. Rep.* **409**, 47–99. https://doi.org/10.1016/j.physrep.2004.10.006 (2005).
44. Zhao, Q. & Wagner, H. D. Raman spectroscopy of carbon–nanotube–based composites. *Philos. Trans. R Soc. A*. **362**, 2407–2424. https://doi.org/10.1098/rsta.2004.1447 (2004).
45. Xuan, S., Wang, Y. X. J. & Yu, J. C. Cham-Fai Leung, K. Tuning the grain size and particle size of superparamagnetic Fe_3O_4 microparticles. *Chem. Mater.* **21**, 5079–5087. https://doi.org/10.1021/cm901618m (2009).
46. Ziegler-Borowska, M., Chełminiak, D., Kaczmarek, H. & Kaczmarek-Kędziera, A. Effect of side substituents on thermal stability of the modified chitosan and its nanocomposites with magnetite.

J. Therm. Anal. Calorim. **124**, 1267–1280. https://doi.org/10.1007/s10973-016-5260-x (2016).

47. Tenório-Neto, E. T. et al. TGA and magnetization measurements for determination of composition and polymer conversion of magnetic hybrid particles. *Polym. Adv. Technol.* **26**, 1199–1208. https://doi.org/10.1002/pat.3562 (2015).
48. Titus, E. et al. Chemically functionalized carbon nanotubes and their characterization using thermogravimetric analysis, fourier transform infrared, and raman spectroscopy. *J. Mater. Eng. Perform.* **15**, 182–186. https://doi.org/10.1361/105994906X95841 (2006).
49. Yadav, M. et al. Heterogeneous cobalt nanocatalyst for reductive transformation of nitroarenes to aryl amines using isopropanol as a hydrogen source. *Ind. Eng. Chem. Res.* **64**, 6771–6787. https://doi.org/10.1021/acs.iecr.4c04023 (2025).
50. Li, S. et al. Synergistic effect of Ru-Ni nanoparticles supported on mesoporous carbon black for highly selective hydrogenation of nitrobenzene to aniline in aqueous phase. *Fuel* **402**, 136060. https://doi.org/10.1016/j.fuel.2025.136060 (2025).
51. Bari, M. A. et al. Iron-catalyzed transfer hydrogenation of allylic alcohols with isopropanol. *J. Org. Chem.* **89**, 14571–14576. https://doi.org/10.1021/acs.joc.4c01701 (2024).
52. Anikeev, V. I. et al. Highly selective reduction of nitroarenes by sc-isopropanol in the presence of zirconia in a flow reactor. *J. Supercrit Fluids*. **140**, 233–237. https://doi.org/10.1016/j.supflu.2018.06.021 (2018).

Tables

Table 1 to 3 are available in the Supplementary Files section.

Figures

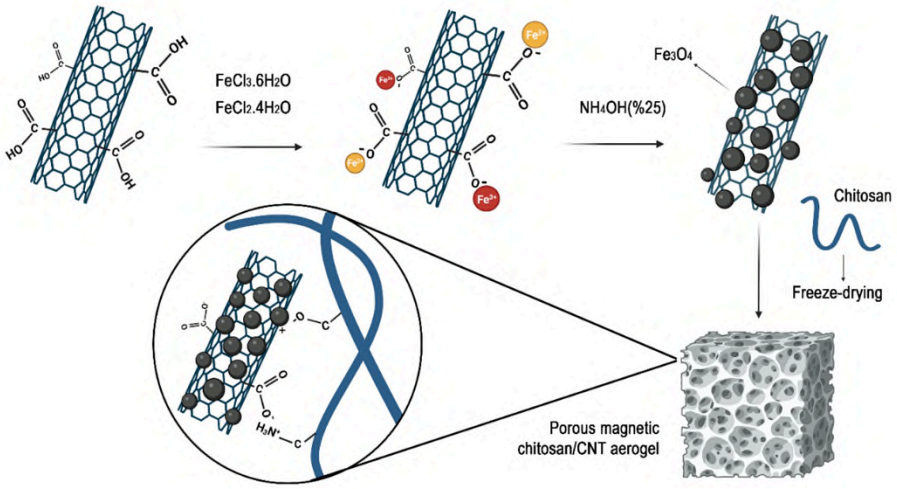


Figure 1. Schematic representation of the synthesis of Fe_3O_4–CNT aerogel

Figure 1

See image above for figure legend

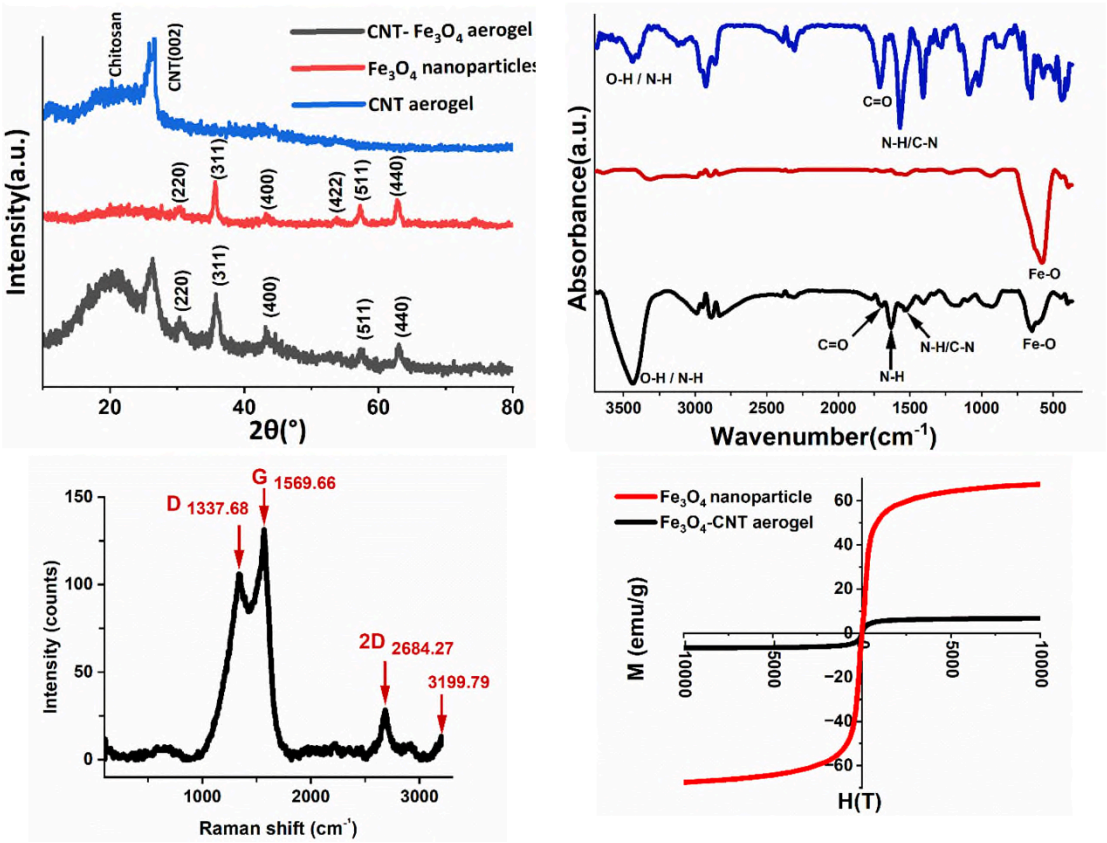


Figure 2. Top left: XRD patterns of CNT arogel, Fe3O4 nanoparticles, CNT-Fe3O4 aerogel; top right: FTIR spectra of CNT arogel, Fe3O4 nanoparticles, CNT-Fe3O4 aerogel; bottom left: Raman spectrum of the Fe_3O_4–CNT aerogel catalyst; Bottom right: Room-temperature VSM hysteresis loops of Fe_3O_4 nanoparticles and Fe_3O_4–CNT magnetic aerogel.

Figure 2

See image above for figure legend

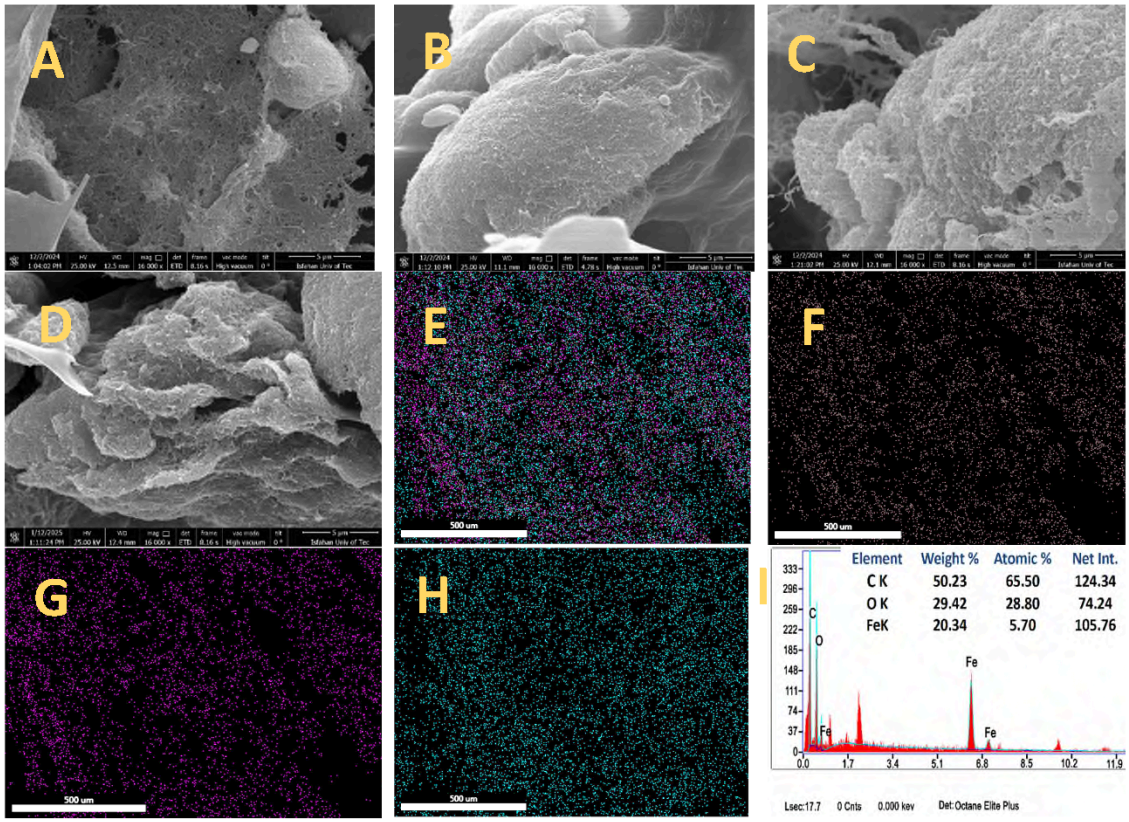


Figure 3. FESEM images of magnetic aerogel samples prepared using different synthesis routes: A) Catalyst A B) Catalyst B C) Catalyst C D) catalyst D; E) The total elemental mapping of catalysts D, in attendant its map of carbon distribution (F), its map of oxygen distribution (G), its map of iron distribution (H), and its EDS analysis (I)

Figure 3

See image above for figure legend

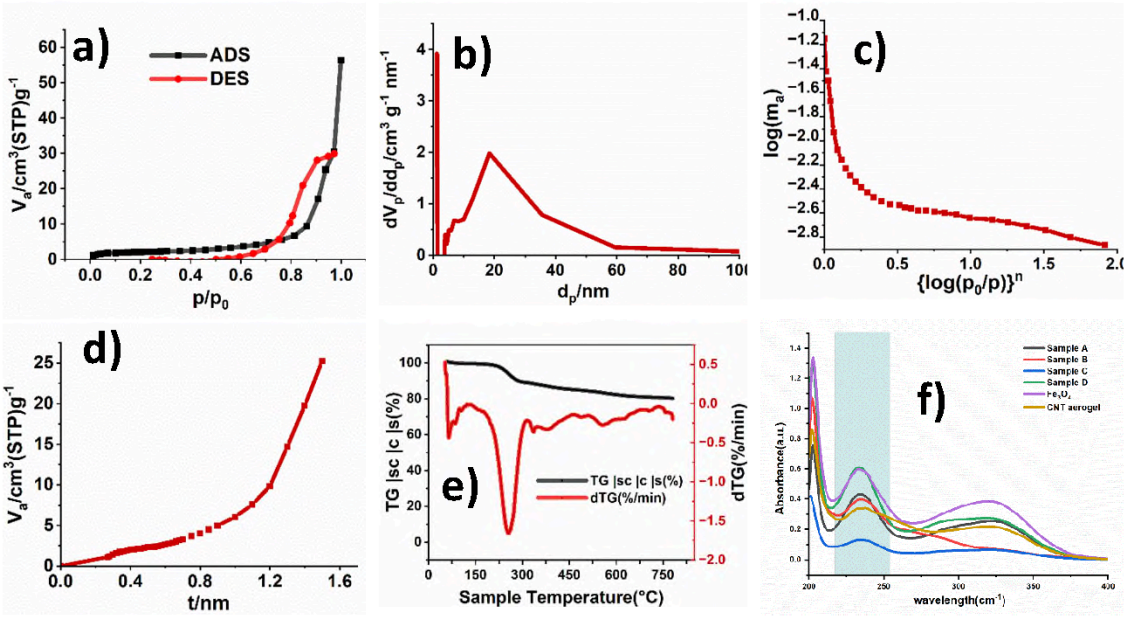


Figure 4. (a) N_2 adsorption–desorption isotherm; (b) pore size distribution calculated by the BJH method; (c) Dubinin–Astakhov (DA) plot; (d) t-plot; (e) TGA and DTG curves of the Fe_3O_4–CNT aerogel, indicating the thermal decomposition steps and corresponding weight-loss rates; and (f) UV–Vis absorption spectra of reaction mixtures obtained using different catalysts under identical reaction conditions.

Figure 4

See image above for figure legend

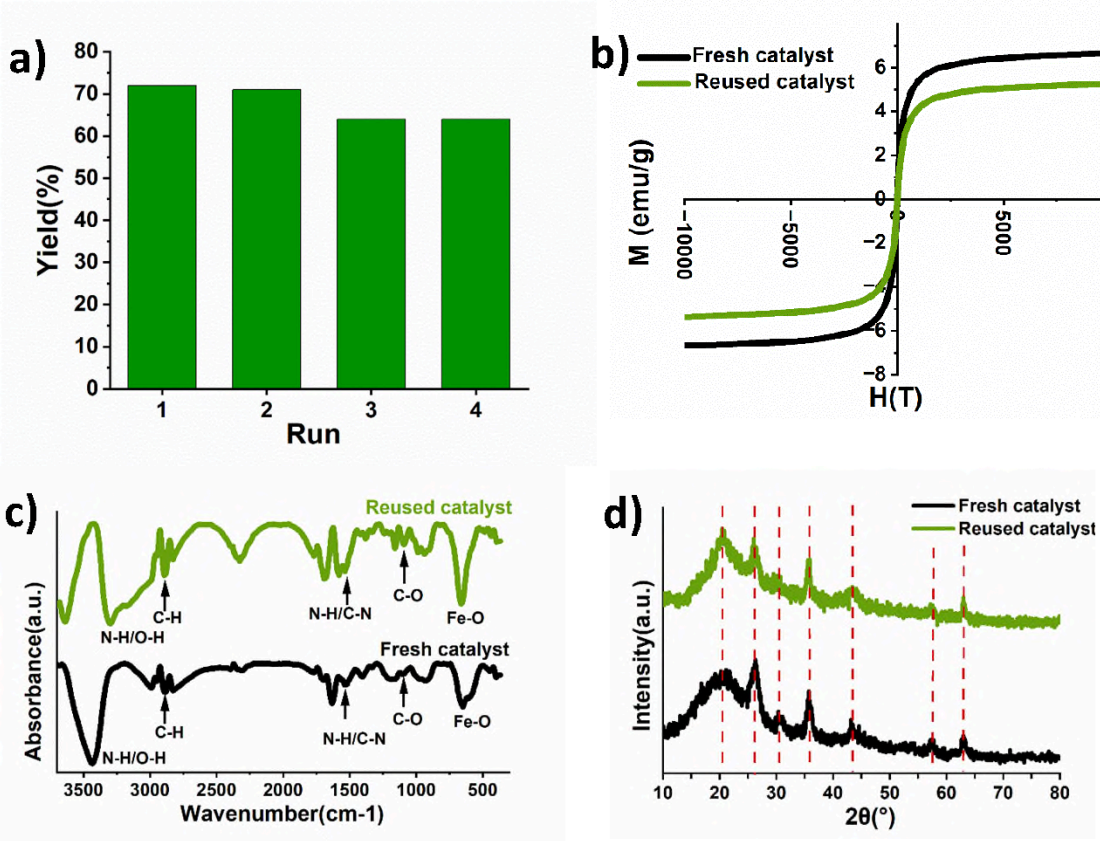


Figure 5. Recyclability and post-reaction characterization of the catalyst.: a) Catalytic performance over four consecutive cycles; b) VSM analysis of the recovered catalyst; c) FTIR spectrum after reuse; d) XRD pattern of the recycled catalyst, confirming structural stability and magnetic integrity.

Figure 5

See image above for figure legend

Supplementary Files

This is a list of supplementary files associated with this preprint. Click to download.

- Supportinginformation.docx
- Tables.docx